Magnetic flux penetration in nanoscale wedge-shaped superconducting thin films

L. B. L. G. Pinheiro,[1,2] L. Jiang,[3,4] E. A. Abbey,[1] Davi A. D. Chaves,[1] A. J. Chiquito,[1] T. H. Johansen,[5] J. Van de Vondel,[6] C. Xue,[7] Y.-H. Zhou,[3,8] A. V. Silhanek,[4] W. A. Ortiz,[1] and M. Motta[1,*]

[1]*Departamento de Física, Universidade Federal de São Carlos, 13565-905 São Carlos, SP, Brazil*
[2]*Instituto Federal Federal de São Paulo, 13565-905 São Carlos, SP, Brazil*
[3]*School of Aeronautics, Northwestern Polytechnical University, Xi'an 710072, China*
[4]*Département de Physique, Université de Liège, B-4000 Sart Tilman, Belgium*
[5]*Department of Physics, University of Oslo, P.O. Box 1048 Blindern, 0316 Oslo, Norway*
[6]*Quantum Solid-State Physics, Department of Physics and Astronomy, KU Leuven, Celestijnenlaan 200D, B-3001 Leuven, Belgium*
[7]*School of Mechanics, Civil Engineering and Architecture, Northwestern Polytechnical University, Xi'an 710072, China*
[8]*Department of Mechanics and Engineering Sciences, Lanzhou University, Key Laboratory of Mechanics on Disaster and Environment in Western China, Ministry of Education of China, Lanzhou 730000, China*

(Received 18 October 2022; revised 9 December 2022; accepted 13 December 2022; published 27 December 2022; corrected 10 February 2023)

Thickness uniformity is regarded as an important parameter in designing thin film devices. However, some applications based on films with nonuniform thickness have recently emerged, such as gas sensors and optimized materials based on the gradual change of film composition. This work deals with superconducting Pb thin films with a thickness gradient prepared with the aid of a diffuse stencil mask. Atomic force microscopy and energy-dispersive x-ray spectroscopy show variations in the range 90 nm–154 nm. Quantitative magneto-optical images reveal interesting features during both the abrupt and the smooth penetration regimes of magnetic flux, as well as the thickness-dependent critical current density (J_c). In addition, we observe a gradual superconducting transition as the upper critical field is progressively reached for certain thicknesses. Furthermore, the hysteresis observed for triggering flux avalanches when increasing and decreasing magnetic fields is also accounted for by the J_c profile evolution along the thickness gradient. Numerical simulations based on the thermomagnetic model are in fair agreement with the experimental data. These findings demonstrate that wedge-shaped films are a viable approach to investigate, in a continuous fashion, thickness-dependent properties of superconducting materials.

DOI: 10.1103/PhysRevB.106.224520

I. INTRODUCTION

Several promising technologies, such as superconducting qubits [1,2] or single photon detectors [3,4], are based on thin films. Nonuniform thickness distributions are described as a common point of concern for different evaporation techniques [5]. In fact, great effort has been exerted to optimize preparation conditions to guarantee uniformity and reproducibility in films used for a large diversity of applications [6–11]. However, it is possible to harness differences in material properties arising from thickness gradients to develop devices with complex responses. For example, the ideal composition of Ti-Ni-based shape memory alloys with near-zero thermal hysteresis was identified and later produced as a bulky material following an approach based on thin-film combinatorial deposition of nanoscale wedgelike multilayers with varying material composition and high-throughput characterization methods [12,13]. Recently, this strategy was also applied to control the Ce doping concentration in the superconductor $La_{2-x}Ce_xCuO_4$ to investigate the anomalous non-Fermi liquid behavior and the mechanism for the superconductivity in those systems [14]. Another example is related to novel gas sensors using thickness gradient films to detect low concentrations of hydrogen and ethanol gases [15,16]. Furthermore, wedge-shaped superconducting-ferromagnetic heterostructures have successfully been used to prepare tunnel junction arrays presenting multiple 0-π transitions [17] and spin-valve cores [18].

For single superconducting layers, specimens with graded thickness or nonuniform critical current density, J_c, have been investigated on a theoretical and numerical basis [19–22]. Exceptionally, Sabatino *et al.* [23] unveiled a directed vortex motion on a uniform film of micrometric dimensions with asymmetric thickness profile edges and confirmed their findings by time-dependent Ginzburg-Landau (TDGL) simulations. Later on, Gladilin *et al.* [24] employed the TDGL formalism to numerically investigate the dynamics of penetrated magnetic flux in a wedge-shaped film made of a type-I superconductor and steep enough to allow the thinnest part to behave as a type-II superconductor. In general, for nonuniform thick samples, there are a number of numerical and experimental investigations pointing to an important thickness dependent $J_c(d)$ [25–32].

For type-II superconductors, critical state models [33–35] are a powerful tool to unveil superconducting properties. They

*Corresponding author: m.motta@df.ufscar.br

state that current flows in the superconductor at its critical value wherever there are vortices penetrated. For the simpler Bean model [33], J_c is independent of the local flux density, B_z, however, a flux-dependent $J_c(B_z)$ may be essential to describe some subtle features [36–39]. In general, knowledge of the flux distribution provides information about the current distribution throughout the specimen [40–44]. The critical state models do not account for all possible scenarios of magnetic flux penetration. This is particularly the case for thin films, for which stochastic abrupt dendritic flux penetration events, known as flux avalanches, take place at low temperatures [45–47]. The origin of such avalanches are thermomagnetic instabilities [46], occurring when the material cannot assimilate the heat generated by vortex motion, thus resulting in a positive-gain feedback loop, which initiates a macroscopic magnetic flux burst characterized by a dendritic pattern.

Despite the unpredictable nature of these catastrophic events, much is known about the general influence of different environmental and sample parameters on their behavior [48,49]. For instance, an increase in temperature leads to fewer but more branched and larger avalanches [50,51]. They are also triggered for lower fields in films decorated with microscopic arrays of defects [47,52]. Besides that, their morphology is profoundly influenced by the geometry of the defect and its lattice symmetry [53]. Film thickness also influences the flux avalanches since thinner samples require a lower applied magnetic field to trigger the first avalanche [54–56]. These abrupt flux penetrations may be detrimental to applications because an avalanche can locally destroy the superconducting state [49]. As such, their understanding is crucial for developing large-area thin superconducting devices. In particular, a comprehensive experimental study about the effects of thickness variation throughout large areas is still lacking.

In this work, we report experimental and numerical investigations on the flux penetration in a type-II superconducting Pb wedge-shaped film of millimetric lateral dimensions. Atomic force microscopy (AFM), energy-dispersive x-ray spectroscopy (EDS), and scanning electron microscopy (SEM) were used to characterize the wedge profile and the structural properties of the sample. The magneto-optical imaging (MOI) technique and numerical simulations based on the thermomagnetic (TM) model shed light on the magnetic flux penetration and the superconducting current distribution as the thickness changes gradually throughout the specimen. Both MOI and TM model reveal the impact of thickness on the avalanche morphology and their dependence on the magnetic history.

II. MATERIALS AND METHODS

A. Sample details

A 2×7 mm^2 Pb film was deposited onto a Si (100) substrate by conventional thermal evaporation with a thickness gradient along its longest dimension. A diffuse-shadow mask was used to create the wedge, spanning the thickness in the range 90 nm–154 nm. A 20 nm-thick uniform protective Ge layer was deposited on top of the film. Microstructural characterization was done by AFM and SEM/EDS. The AFM images were captured in the peak-force tapping mode using a Digital Instruments Nanoscope V. The SEM/EDS measurements were carried out in a Philips XL-30 FEG Scanning Electron Microscope together with a XFLash 6/60 Bruker x-ray detector. Details of the sample fabrication and SEM/EDS analyses are presented in Appendixes A and B, respectively.

Additionally, samples with different geometries and thickness gradients, oriented along the edges and diagonally to the edges of the samples, were fabricated and investigated. The results obtained reproduce and confirm those described in this work. For clarity, the discussion is focused on the rectangular wedge-shaped film described in the previous paragraph, which presents the largest variation of the superconducting properties.

B. Quantitative MOI

The MOI technique is employed to visualize the spatial distribution of penetrated flux in the nanoscale wedge-shaped superconducting film. This technique relies on the Faraday effect in an indicator film, where polarized light will have its polarization rotated proportionally to the local magnetic field in the indicator, placed on top of the superconducting specimen. The indicator used in the present work is a Bi-substituted yttrium iron garnet film (Bi:YIG) with in-plane magnetization, covered with a 100 nm-thick Al mirror [57,58]. The resulting magneto-optical (MO) images are captured by a charge-coupled device (CCD) camera and show a qualitative magnetic flux distribution throughout the superconducting film, where the local brightness is related to the magnitude of the perpendicular flux density. A quantitative $B_z(x, y)$ picture is obtained using a pixel-by-pixel calibration algorithm implemented on MATLAB [59]. We also correct for sample drift with a precision of ±2 pixels (or ±8.3 μm) in the position of any given image during the runs by employing the plug-in STACKREG [60] together with IMAGEJ software [61]. The two-dimensional current distribution can be obtained from $B_z(x, y)$ by making a numerical inversion of the Biot-Savart law. In our case, we used the algorithm provided by Meltzer *et al.* [62].

The critical temperature of a sister sample from the same batch, determined in a Quantum Design MPMS-5S magnetometer using ac susceptibility measurements, is $T_c = (7.20 \pm 0.05)$ K, whereas T_c determined by the uniform lack of image contrast using the MOI is $T_c^{\mathrm{MOI}} = (5.1 \pm 0.1)$ K, as presented in Appendix C. This difference is a consequence of a nonoptimum thermal contact between the sample and the cold finger. In order to obtain a meaningful comparison between MOI data and numerical simulations, the former is expressed in units of reduced temperature T/T_c^{MOI} and the latter in $t = T/T_c$.

C. Numerical simulations

The magnetic flux penetration in the wedge-shaped superconducting Pb films is further numerically investigated by the TM model [46,50,63], providing deeper insight into the observed thickness-dependent characteristic of the flux instabilities. Here, we consider a superconducting film with

length of $2L = 7$ mm and width of $2W = 2$ mm, the same as the deposited film, and space-varying thickness $d(x, y)$. The sample is zero-field cooled (ZFC) to a base temperature T_0. The nonlinear material characteristics of the superconductor are described by the general $E - j$ constitutive law:

$$\mathbf{E} = \begin{cases} \rho_n (j/dJ_c)^{n-1}\mathbf{j}/d & \text{if } j < dJ_c \text{ and } T < T_c, \\ \rho_n \mathbf{j}/d & \text{otherwise,} \end{cases} \quad (1)$$

where ρ_n is the normal state resistivity, $\mathbf{j}$ is the sheet current, which is defined as $\mathbf{j}(x, y) = \int_{-d/2}^{d/2} \mathbf{J}(x, y, z)dz$, and n is the flux creep exponent. The temperature dependencies are $J_c = J_{c0}(d)(1 - T/T_c)$ and $n = n_0 T_c/T - 50$ [53]. The J_c dependency on thickness across the sample has been taken from the experimental results as will be explained in the next section.

The electrodynamics of the superconducting thin film exposed to a transverse magnetic field follows Maxwell's equations:

$$\dot{\mathbf{B}} = -\nabla \times \mathbf{E}, \ \nabla \times \mathbf{H} = \mathbf{j}\delta(z), \quad \text{and } \nabla \cdot \mathbf{B} = 0, \quad (2)$$

with $\mathbf{B} = \mu_0 \mathbf{H}$, and $\nabla \cdot \mathbf{j} = 0$. Thermomagnetic instabilities resulting from coupling the nonlinear electromagnetic characteristics of superconductors and the Joule heating created by magnetic flux motion. Thus the electrodynamics is supplemented by the heat diffusion equation

$$dc\dot{T} = d\kappa \nabla^2 T - h(T - T_0) + \mathbf{j} \cdot \mathbf{E}, \quad (3)$$

where, κ, c, and h are the thermal conductivity, the specific heat, and the coefficient for heat removal to the substrate, which are all assumed to be proportional to T^3. The terms on the right side of Eq. (3) are related to the heat conduction within the film, heat flow to the substrate, and positive feedback due to Joule heating, respectively. A flux avalanche will occur if the superconductor cannot evacuate heat fast enough, triggering a positive-gain feedback loop depending on the relative significance between the magnetic flux diffusion (D_m) and the thermal diffusion (D_t) coefficients [64]. The key parameter controlling the occurrence of avalanches is given by $\tau = D_t/D_m = \mu_0 \kappa_0 \sigma / c$.

We solve Eq. (3) together with Eqs. (1) and (2), using a real space/Fourier space hybrid method proposed by Vestgården *et al.* [50] with boundary conditions with $j = 0$ outside the superconducting film. The parameters used in the simulation are related to Pb films [65]: $T_c = 7.2$ K, $\rho_n = 5.7\times10^{-9}$ Ωm, $\kappa(T = T_c) = 20$ W/Km, $c(T = T_c) = 3\times10^4$ J/Km^3, and $h(T = T_c) = 1\times10^4$ W/Km^2. We choose $n_0 = 90$ and limit the creep exponent to a maximum value of $n_{\max} = 100$.

III. RESULTS AND DISCUSSION

An important first step consists in characterizing the structure of the wedge-shaped films from millimetric down to nanoscopic scales. Figure 1(a) shows an optical image of the rectangular film with reasonably well-defined edges and the five regions where the thickness variation was investigated, indicated by colored square boxes. Representative thickness profiles obtained from AFM images are presented in Fig. 1(b). The thickness values for each region, represented by the colored dashed lines, were evaluated by averaging six different

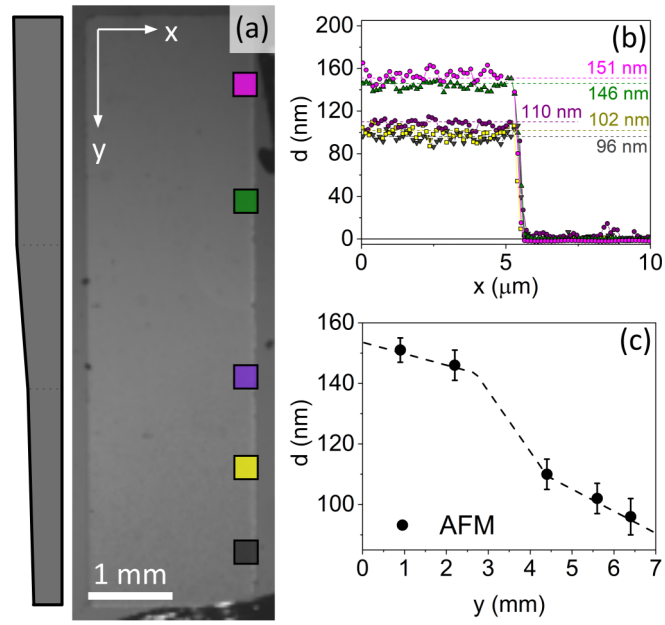

FIG. 1. Sample characterization. (a) Optical image of the wedge-shaped film, which shows five regions along the y axis where the thickness was determined. (b) Representative thickness profiles for the different indicated sample regions taken from AFM images. Dashed lines correspond to the averaged thickness over different profiles. (c) Thickness versus y position obtained from the AFM data. The dashed black line is the thickness used in the numerical simulations. The gray-black vertical bar at the left side of (a) is a pictorial representation of the thickness variation along the wedge.

profiles and present standard deviations between 4 nm and 6 nm. To evaluate these Pb thicknesses, we subtract 20 nm referent to the Ge layer. Figure 1(c) shows the film thickness versus vertical position obtained from the AFM data. The dashed lines are an approximation of the real thickness profile and were used in the numerical simulations. The microstructure and thickness evolution throughout the film are corroborated by SEM images and EDS spectra, as shown in Appendix B.

The flux distribution along the gradient film was investigated by MOI, as shown in Figs. 2(a)–2(d) at constant temperature $t = 0.59$ and for increasing applied fields after a ZFC procedure. All MO images in this work had their contrast adjusted to prevent overexposure. Below each image, a color bar quantifies B_z throughout the sample. The gray smudge at the left side represents a region where vacuum grease unexpectedly jumped from the cold finger assembly during the experiment. Its gray level was kept constant for all MO images throughout the text. Fortunately, the smudge lies above the MO indicator and does not affect the response of the sample. The flux penetration observed at this temperature is as described by the critical state models [33,34,66]. In the top thicker half of the sample, the flux front penetrates deeper and becomes more apparent above $H = 22$ Oe. Consequently, its shielding capability is inferior to that of the bottom half (thinner region). In addition, the flux fronts on the left and right borders close to the top and bottom edges are affected as a consequence of the supercurrents, which have to adapt to the

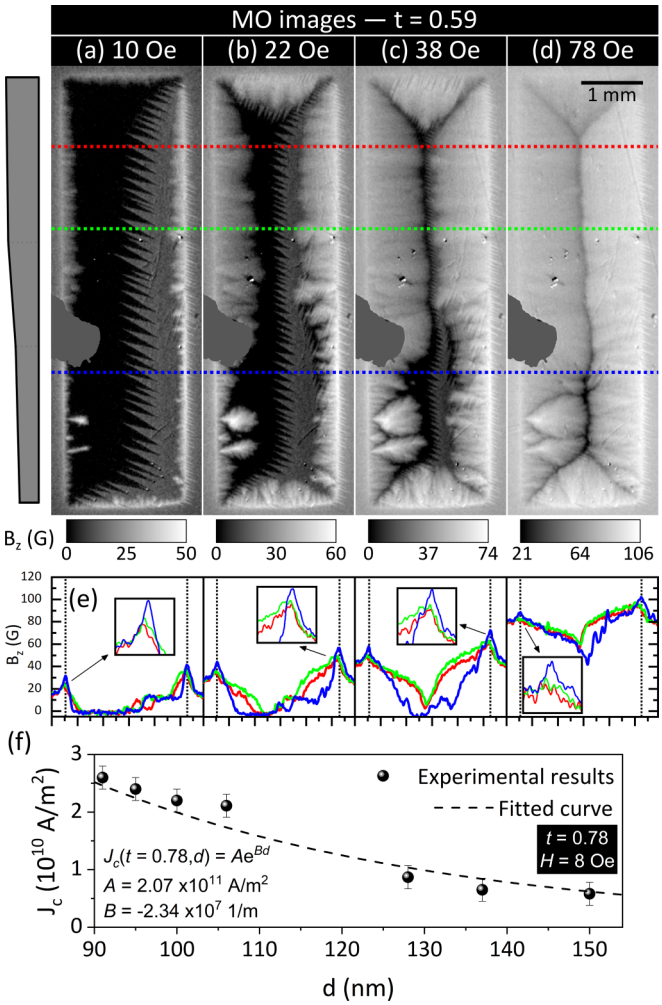

FIG. 2. MO images of the smooth flux penetration for wedge-shaped rectangular film captured at $t = 0.59$, after ZFC and for increasing H: (a) 10 Oe, (b) 22 Oe, (c) 38 Oe, and (d) 78 Oe. (e) B_z profiles taken along the colored dashed lines in the MO images. The insets show details of B_z around the edges of the film. (f) Thickness-dependent critical current density at $t = 0.78$ and $H = 8$ Oe, obtained by the flux front position along vertical left edge using the approximation given by Eq. (4). The dashed line is an exponential fit of the experimental data, with parameters presented in the figure.

rectangular geometry of the film, resulting in black diagonal lines, also known as discontinuity lines or d lines [67]. The vertical d line emerges gradually when the field reaches the center of the film, even though the flux front depth is not homogeneous and the full penetration field is not unique. Figures 2(a)–2(d) were selected to highlight the difference among the thicker and the thinner regions of the specimen. The fact that we do not observe additional symmetrical d lines anywhere in the film [53,68] is a strong indication that there exists a smooth thickness gradient, as represented in Fig. 1(c). It is important mentioning that two flourishing patterns on the bottom left edge are due to defects, which favor the flux penetration around them [69] and produce a minor distortion of the central d line and a slight asymmetry of the side borders. This type of nonuniform flux penetration due to a thickness variation has been also observed in a V_3Si film [70]. Figure 2(e) shows examples of the spatial profile of the induction component B_z taken for different applied fields, being obtained from the average on a 208-μm-wide strip around the colored horizontal dashed lines depicted in Figs. 2(a)–2(d). They present the typical critical statelike profile for different fields, showing the flux penetration progression for each region. The zigzag patterns, mainly on the right half of the sample, are due to domain boundaries in the MO indicator and have little effect on the flux distribution in the superconducting film. They also become visible as an asymmetry between the peaks on the left and the right edges and in the shielded portion in the flux-free Meissner region up to 38 Oe. Furthermore, the blue line shows a less pronounced penetration due to the thinner local thickness. Another consequence of this thickness modulation within the sample becomes apparent in the insets of Fig. 2(e): a higher B_z is observed across the edges of the wedge-shaped film for lower thicknesses. These facts indicate the prominent role played by demagnetization effects on the sample behavior [41,44]. One immediate effect of such flux penetration pattern is that this difference in B_z is intrinsically linked to the superconducting shielding currents across the film. Therefore, demagnetization effects are a key ingredient in explaining the thickness-modulated superconducting properties presented by our sample.

In order to crudely estimate the critical current density (J_c) at different vertical positions, the flux front penetration depth may be evaluated using MO images. Considering the Bean model [33,66] for uniform thin films with stripe geometry, J_c is given by [44,71]:

$$J_c = \frac{\pi H}{d\,\mathrm{acosh}\left(\frac{W}{W-a}\right)}, \tag{4}$$

where a is the flux front penetration depth measured from the long edges. An example of this estimation is given in Fig. 2(f) for $t = 0.78$ and $H = 8$ Oe. The thickness dependence described by Eq. (4) arises from geometrical considerations for an infinitely long stripe [44]. However, this equation does not explicitly take into account the thickness dependence on a. For this reason, we have empirically approximated J_c by an exponentially decaying function of film thickness. This behavior was also reported by Foltyn *et al.* for YBCO [72] and Huebener and Seher for Pb [73], but in those cases for uniform films, each with a different thickness. Therefore, decreasing the thickness makes the superconducting film more capable of self-shielding [44,74]. The contrast in MO images is a consequence of the penetrated flux and supercurrent density distributions throughout the superconductor [75]. Thus, when the superconductor undergoes a phase transition to the normal state, no contrast throughout the image can be recognized. Hence, the critical temperature was determined by MOI in a temperature sweep at zero field after a field cooled (FC) procedure at $H_{FC} = 20$ Oe. For the wedge-shaped film, the image contrast vanishes homogeneously (see Appendix C) at a single T_c, since there is no significant thickness dependence of T_c in the investigated range (90 nm–154 nm) for Pb films [76,77]. Alternatively, the specimen can also undergo a transition to the normal state above the upper critical field (H_{c2}) at a certain temperature. Figures 3(a)–3(d) show MO images taken at $t = 0.78$ for applied fields higher than the

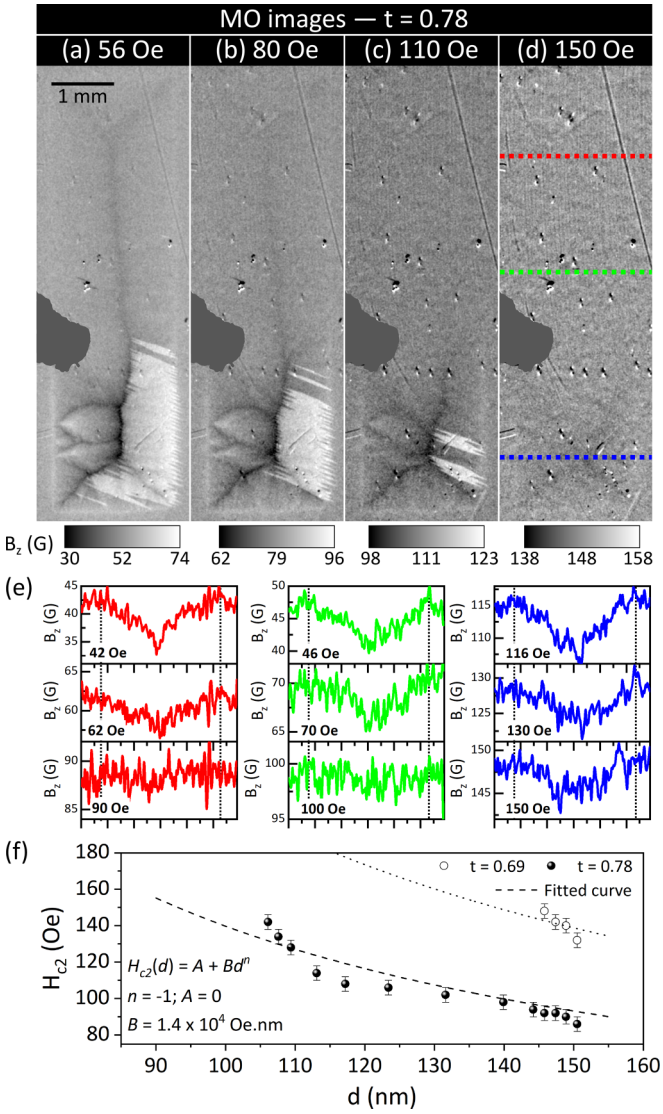

FIG. 3. MO images of the smooth flux penetration obtained at reduced temperature $t = 0.78$ and applied fields of (a) 56 Oe, (b) 80 Oe, (c) 110 Oe, and (d) 150 Oe. (e) Flux density profiles taken along the colored dashed lines depicted in (d) for different applied fields. (f) Thickness-dependent upper critical field at reduced temperatures of $t = 0.69$ and $t = 0.78$ obtained by the analyses of the B_z profile curves.

full penetration field throughout the film after a ZFC procedure. One can observe that the thicker region of the specimen fades out when compared to the thinner part. In Fig. 3(a), four current domains are separated by two *V*-shaped d lines in the extremes and a nearly vertical d line in the center of the film. At 80 Oe [Fig. 3(b)], the borders of the upper part of the sample practically vanish, but the top *V*-shaped d line can still be barely discerned together with the vertical one. At a higher field (110 Oe), one can distinguish the persistence of the superconducting state only below the smudge, thanks to the flux distribution and the d lines. The evolution of these upper d lines can be seen in Fig. 3(d), taken at 150 Oe, where a *X*-shaped d line can still be recognized. These observations demonstrate that the upper critical field depends inversely on the film thickness and reinforces the role played

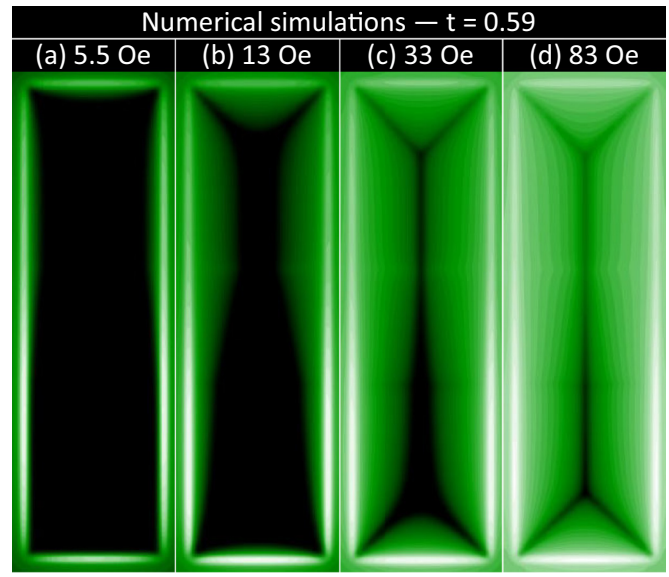

FIG. 4. Simulated distribution of B_z in a wedge-shaped superconducting film at $t = 0.59$ after an applied magnetic field from zero to (a) 5.5 Oe, (b) 13 Oe, (c) 33 Oe, and (e) 83 Oe. The image brightness represents the magnitude of B_z. The images show a deeper and a less pronounced flux front penetration on the upper region and lower region of the sample, respectively, similar to the MO observations.

by the thickness variation on the superconducting properties of thin films.

To obtain $H_{c2}(d)$ curves at different temperatures, flux density profiles along the sample width were analyzed for several thicknesses. Figure 3(e) shows examples of the spatial profile of B_z for different fields, being obtained from the average on a 208-μm-wide strip around the colored horizontal dashed lines depicted in Fig. 3(d). At low fields, the Bean-like profile can be recognized for all regions despite restrictions related to the experimental uncertainty that has a standard deviation of 4 G [39]. As the applied field is increased, the B_z profile becomes flatter, however, a slope towards the center of the sample can still be perceived. When the upper critical field H_{c2} is reached, a roughly position-independent B_z profile takes place as, for instance, in the red and green profiles for 90 Oe and 100 Oe, respectively. By identifying H_{c2} at different thicknesses, a curve of the upper critical field versus thickness can be plotted. Figure 3(f) shows the $H_{c2}(d)$ taken from the MO images at reduced temperatures of 0.69 and 0.78. Despite a relatively important uncertainty in the obtained results, the data set for $t = 0.78$ (closed circles) suggests that H_{c2} and d are inversely proportional. A similar $H_{c2} \propto d^{-1}$ behavior was also observed for uniform-thickness Pb films [78,79] and for films made from other metals and alloys [78,80–82]. The data at $t = 0.69$ (open circles) is limited by the maximum available magnetic field at our MOI setup (150 Oe). Nevertheless, an inverse proportionality between H_{c2} and d is also observed at that temperature.

In order to further analyze the experimental MO results, we have simulated a wedge-shaped superconducting film using the TM model framework [50,63], considering the experimental $J_c(d)$ profile presented in Fig. 2(f). Figure 4 presents

the distribution of magnetic flux density B_z at [Fig. 4(a)] 5.5 Oe, [Fig. 4(b)] 13 Oe, [Fig. 4(c)] 33 Oe, and [Fig. 4(d)] 83 Oe. The substrate temperature was kept at $t = 0.59$. In this case, regions where magnetic flux is absent appear as black, whereas maximum field corresponds to the brightest intensity. The main features observed experimentally in Fig. 2 are captured by the numerical simulations. In the thicker region on the upper edge, the flux front penetrates deeper and reaches the sample center at around 20 Oe. The flux front in the bottom region, where the supercurrent density is higher, achieves the condition of full penetration at 55 Oe, presenting a better shielding, as in the experiments.

Another interesting feature is the inhomogeneous brightness along the perimeter of the sample. The lower region of the rim is brighter due to a better shielding ability (higher J_c), leading to a higher concentration of magnetic flux at the edges. This increase in the brightness along the bottom rim of the sample is also observed for the MO images, which can be observed in the zoom of the B_z profiles close to the edges in Fig. 2(e).

Besides the described smooth flux penetration, when the magnetic diffusion is faster than the thermal diffusion, thermomagnetic instabilities may develop and cause flux avalanches [64]. This abrupt penetration regime should also be affected by the thickness gradient. Precisely, it corroborates the previous analysis of J_c distribution throughout the specimen, where one expects to trigger more flux avalanches along the edges with higher J_c [47,52]. Figure 5 shows a series of MO images taken at $t = 0.48$ after a ZFC procedure and slowly increasing the applied field up to 150 Oe and then decreasing it to negative values. For increasing fields, the penetration pattern is nonuniform as flux avalanches are nucleated in the thinner region only, whereas from the upper thicker part the penetration is smooth. It is somehow similar to the intriguing effect observed by Albrecht *et al.* [83] for a MgB_2 film grown onto a vicinal substrate, which results in a current anisotropy of 6% among the edges. Numerical simulations using TM model also presented such avalanche preferential propagation [84] for different current anisotropies. This phenomenon also appears for the wedged-shaped film, which has a difference of around 400% in J_c between the thinner and thicker regions.

The morphology of the flux avalanches depends strongly on the temperature, as reported by several authors [50,52,55,85–87]. Our results show that even for a fixed temperature, but under different conditions of H and J_c modulated by the thickness variation, the morphology of the avalanches depends on thickness. Figure 5(a) shows the first avalanches nucleated exclusively at the thinner region of the sample, where J_c is higher. In this case, the dendrites present many long and thin fingerlike patterns, almost without ramifications. At 32 Oe, branched medium-sized dendrites for thicknesses around 105 nm (2 mm above the bottom edge) and new longer fingers at the lower part emerged. For an applied field of 66 Oe, even larger and more branched dendrites occur whereas the thicker part develops the critical statelike penetration. Another important feature of the avalanches in Fig. 5(c) is their size and the bending of their ramifications toward the thicker zone. In other words, when a region of the sample has no avalanches yet, the first branches point

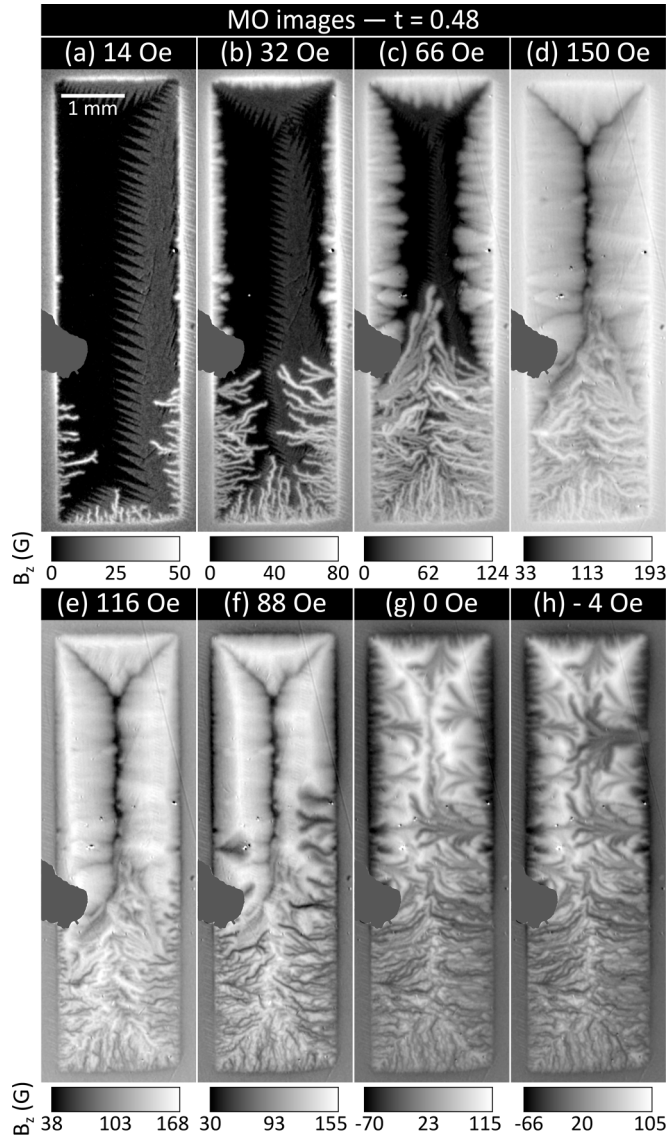

FIG. 5. MO images of the abrupt penetration of flux avalanches taken at $t = 0.48$ and fields of (a) 14 Oe, (b) 32 Oe, (c) 66 Oe, and up to (d) 150 Oe, after a ZFC procedure. Then, the field is decreased down to (e) 116 Oe, (f) 88 Oe, (g) 0 Oe (the remnant state), and (h) −4 Oe.

towards the center of the sample, as expected. However, avalanches triggered at higher fields close to the thicker zone deviate and propagate towards the flux-free Meissner region. A possible explanation for this effect relies on the fact that avalanches avoid crossing the existing ones, as described earlier by Johansen *et al.* [88], and there is still flux-free area in the thicker region, while the thinner region is already filled with previously triggered flux avalanches. Similar behavior has also been observed in a work by Choi and coauthors [89] in which avalanches bend around a gold rim covering only half of a MgB_2 film. Figure 5(d) illustrates the coexistence of the smooth penetration and the avalanche regimes in a single sample: at the upper half of the film the flux front already reached the full penetration state whereas avalanches keep on developing in the thinner part. In this case, some branches are

supplanted by the Bean-like penetration around the grayish spot. It is also important to mention that avalanches are not triggered in the thicker zone as a consequence of the lateral heat diffusion, which is larger for this portion, suppressing the occurrence of avalanches [87].

Additionally, as the critical current density is thickness dependent, the field needed to trigger avalanches increases for increasing thicknesses, as found by Vestgården and coauthors [55]. Considering the $J_c(d)$ dependency for the wedge-shaped film and that the thicknesses where avalanches occur in the range 90 nm–105 nm (a variation of 17%), an important ingredient for the above described avalanche morphology is the flux front penetration depth before its occurrence at each position y (or thickness) [87]. In other words, the deeper initial penetration produces larger and more branching avalanches.

Contrary to Albrecht *et al.* [83] findings in MgB_2 films with anisotropic pinning, nonuniform flux penetration is hysteretic for decreasing fields after a maximum of 150 Oe, i.e., negative field-polarity avalanches (or antiavalanches) are triggered throughout all four sample edges and their morphologies change between the thinner and thicker parts. In this case, antiavalanches nucleate and propagate into the film already populated by positive flux trapped by the pinning centers, still leaving an imprint of positive induction field B_z for $H > 0$ [90]. Figures 5(e)–5(h) show antiavalanches for 116 Oe, 88 Oe, the remnant state, and −4 Oe, respectively. Fingerlike antidendrites are triggered along the thinner edges, whereas medium-sized dendrites are nucleated in the middle of the film where only smooth penetration took place for increasing fields. At the remnant state and −4 Oe, several highly branched antidendrites can be seen along all edges, even at the top one, showing an interesting hysteresis in the flux penetration for increasing and decreasing applied magnetic fields.

Figure 6 shows the simulation results for the avalanche regime. At lower fields (7.3 Oe and 10 Oe) after a ZFC procedure, avalanches are triggered in the thinner portion and present a fingerlike shape, whereas at intermediate fields (12 Oe) a branched avalanche is triggered on the left edge. Further avalanches are nucleated at the maximum field of 15 Oe and the Bean-like penetration develops along the upper part of the sample. For decreasing fields, the region out of the sample becomes dark, the field B_z is negative below 6.6 Oe and some small fingerlike antidendrites are triggered on the thinner zone at the remnant state. At negative applied fields, additional antidendrites with finger shape are nucleated along the thinner region and branched antiavalanches are also triggered on the thicker region, one of them where the critical state was established previously. Therefore, the overall features of the flux avalanches were confirmed by numerical simulations.

The hysteresis between both branches of applied field for triggering flux avalanches can be explained based on the magnetic properties of type-II superconductors together with the TM model. Figure 7 shows current maps and profiles acquired from MO images and simulations for the graded-thickness film. The experimental result was obtained after the transformation from B_z to J maps calculated using the algorithm proposed by Meltzer and coauthors [62], considering the proper thickness profile shown in Fig. 1(c). Moreover, we chose the MO image taken at $t = 0.78$ and $H = 2$ Oe

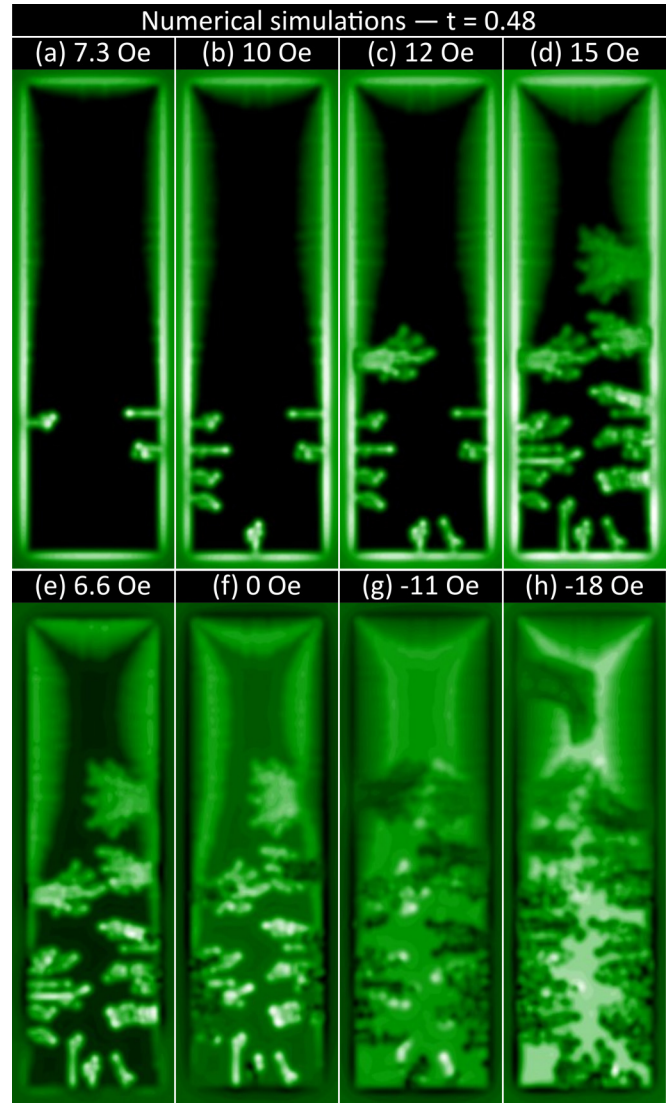

FIG. 6. Simulated flux penetration into the wedge-shaped film obtained at $t = 0.48$ for applied fields gradually increasing to (a) 7.3 Oe, (b) 10 Oe, (c) 12 Oe, (d) 15 Oe, after a ZFC procedure. Then, the field is decreased down to (e) 6.6 Oe, (f) the remnant state (0 Oe), (g) −11 Oe, and (h) −18 Oe.

to minimize artifacts caused by the presence of zigzag domains in the MO indicator. For increasing fields, the shielding current is mainly confined along the perimeter where the magnetic flux is penetrated and decreases towards the center of the sample, as depicted in Fig. 7(a) for both experimental and simulation data. For decreasing fields after a maximum value high enough to reach the full penetration state, a more complex scenario develops because of the flux penetration and the currents throughout the film. Although in the experimental MO image for decreasing fields, garnet domains along the flux front and defects on the edges affect the results, the comparison to numerical calculations yields a satisfactory correspondence for both increasing and decreasing fields.

Figure 7(b) shows J profiles taken along the white vertical dashed line close to the right edge of the sample. The comparison between simulation and experimental data

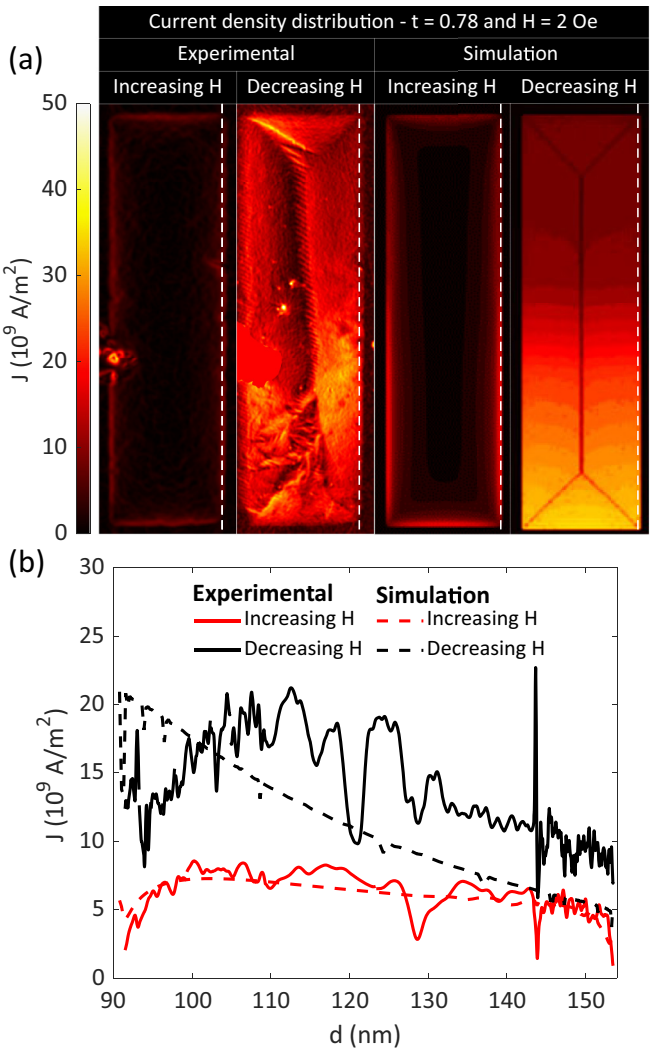

FIG. 7. Current maps and profiles captured at $t = 0.78$ for the wedge-shaped film. (a) Experimental and theoretical current maps at 2 Oe, after a ZFC procedure for increasing field, and at the same H after a maximum value of 150 Oe (decreasing field). A solid red smudge at the second panel covers the region where vacuum grease unexpectedly jumped from the cold finger during the experiment. (b) Thickness dependent current for increasing and decreasing fields, after a maximum of 150 Oe, both taken at 2 Oe, along the white vertical dashed line close to the right edge of the film.

indicate a good agreement despite the large fluctuations observed in the latter. These fluctuations arise from nonuniform flux penetration due to imperfections on the edges. The main observed feature is that both experiment and simulation show an enhancement of the current density at same H during the decrease of the applied field. It is important to note that the experimental J profiles are obtained directly from the MO images, being not related to the critical state models. This explains the discrepancy between experimental and simulation data for decreasing H. For the latter, J is bound by the exponential relationship revealed for $J_c(d)$ in Fig. 2(f), as the simulations do not account for an existing $J_c(B)$ dependency.

Based on these J profiles, avalanches are triggered in thicker regions for decreasing fields in part as a consequence of a higher local J. An important ingredient in this case is the positive feedback due to Joule heating, which depends strongly on the critical current density [87]. This hysteresis in the threshold fields for the occurrence of flux avalanches was first described by Qviller *et al.* [91]. The main idea is related to the difference between the applied field H and the local field B_z close to the edges where avalanches are usually nucleated. Once the field is reduced after a maximum value, the currents close to the edges reverse and B_z reaches a minimum value for a higher value of H in this branch when compared to increasing fields, resulting in higher $J_c(B_z)$ curves for decreasing applied fields. Therefore, the hysteresis between the increasing and decreasing fields for triggering flux avalanches can be completely understood based on the TM model, as well as the regions where avalanches are triggered and their huge diversity in morphology.

IV. CONCLUSIONS

In summary, we successfully prepared a rectangular wedge-shaped film of Pb employing shadow-mask evaporation. We observed a strong $J_c(d)$ dependency, as the critical current increased by over a factor of four when going from the thicker (154 nm) to the thinner (90 nm) edge. When the upper critical field is reached for a certain thickness, the superconducting region undergoes a transition to the normal state revealed by a constant value of B_z along the width of the film. Moreover, the variation of J_c with thickness promotes a great diversity of flux avalanche patterns at a fixed temperature. Based on quantitative MOI, the hysteresis of J profiles for increasing and decreasing applied fields explains the occurrence of antiavalanches in the upper half of the specimen. Taking into account the experimental $J_c(d)$ curve, the numerical simulations based on the TM model presented a consistent correspondence with the experimental results.

These findings show that fabricating wedge-shaped specimens, i.e., exhibiting a thickness gradient, is an interesting strategy to investigate in one and the same sample the material properties dependent on thickness. For superconductors, J_c, H_{c2}, as well as pinning properties can be modulated with suitable thickness. This possibility is enticing for applications. For instance, a thickness-graded superconducting film could be used as a magnetic field sensor. This technology would be based on the sample's progressive transition to the normal state, $H_{c2}(d)$, causing such a film to present a detectable field-modulated resistance.

ACKNOWLEDGMENTS

This work was partially supported by the São Paulo Research Foundation (FAPESP, Grant No. 2021/08781-8), the National Council for Scientific and Technological Development (CNPq, Grants No. 433700/2018-1, No. 431974/2018-7, No. 316602/2021-3, and No. 309928/2018-4), and Coordenação de Aperfeiçoamento de Pessoal de Nível Superior-Brasil (CAPES)-Finance Code 001. This work was also supported by the Research Foundation-Flanders (FWO, Belgium), Grant No. G0A0619N, by the Fonds de la Recherche Scientifique - FNRS under the program PDR T.0204.21, and by COST (European Cooperation in Science

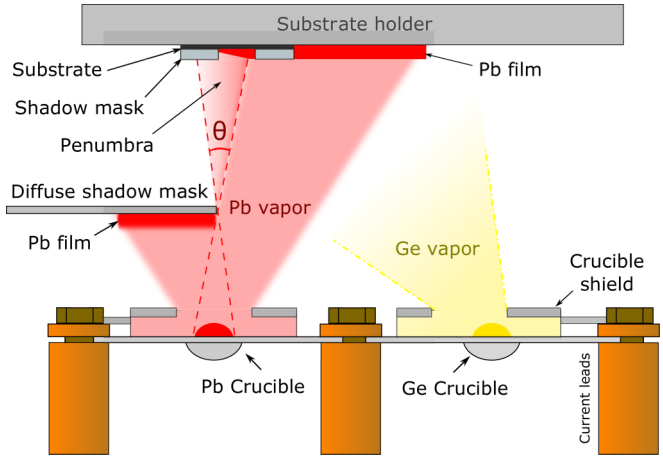

FIG. 8. Schematic diagram of the interior of the thermal evaporator chamber. There is a diffuse-shadow mask between the Pb crucible and the substrate holder to produce a penumbra region where a film with thickness gradient is grown. This image is out of scale.

and Technology) through COST Action CA21144 "SUPERQUMAP". C.X. and L.J. acknowledge the support by the National Natural Science Foundation of China (Grant No. 11972298). L.J. was supported by the China Scholarship Council. The authors would like to thank Laboratory of Structural Characterization (LCE/DEMa/UFSCar) for grating use of its facilities. L.B.L.G.P. and L.J. contributed equally to this work.

APPENDIX A: WEDGE-FILM DEPOSITION

A new all-metal high vacuum chamber was developed to deposit Pb films employing the conventional thermal evaporation technique [92] to achieve controllable conditions to grow low melting point metals. Pb films were fabricated by evaporating 99.999% pure lead placed in a tungsten boat onto a Si (100) substrate. A base pressure of 8×10^{-7} torr is achieved using a liquid-nitrogen cold trap far from the steady substrate holder, which was kept at room temperature. Due to the quick degradation and short lifetime of Pb when exposed to air, a cap layer of Ge was deposited to protect it against oxidation. Throughout the deposition, a quartz crystal microbalance (QCM) based on the OpenQCM project [93] was used to monitor the film thickness during deposition.

To avoid contamination during the film deposition, target metals and substrates were cleaned by chemical wet etching. We prepared the following solutions: HF:HNO_3 with volume ratio of 1:1 for Ge; CH_3COOH:H_2O_2 with ratio 1:1 for Pb; and Piranha etch for the Si wafers [94].

In order to produce a wedge-shaped thin film, a diffuse-shadow mask (DSM) was built and placed inside the chamber between the Pb crucible and the substrate holder, as illustrated in Fig. 8. On the left, the Pb vapor is partially blocked by the crucible shield. The DSM is placed partially covering the Pb crucible, which takes advantage of the nonpunctual vapor source to create an area of penumbra identified by θ and delimited by the dashed red lines delineating the Pb atom paths traced from the extremes of the crucible dip to the substrate holder. Red color indicates the uniform and the wedge-shaped deposition regions for Pb, just below the substrate holder as well as below the DSM. The position of the crucibles in relation to the shields and shutters was made to enable the protective Ge vapor to cover all the wedge-shaped deposition zone. By varying the distance between the DSM and the substrate holder, we are capable of controlling the area of penumbra, i.e., the wedge-shaped deposition zone, and thus change the thickness gradient.

To delineate the edges, another shadow mask was directly clamped to the substrate. Thus, the resulting film has a rectangular shape of area 2×7 mm^2 and the thickness gradient along the major length.

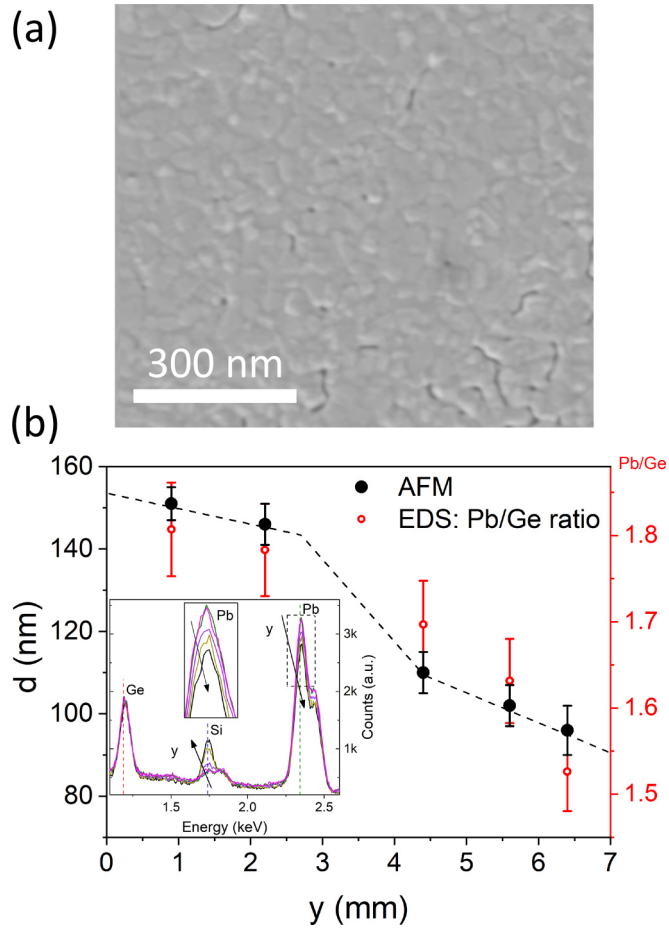

FIG. 9. (a) Secondary electron SEM image of a coevaporated sample. (b) Intensity ratio of Pb/Ge is plotted in red in the main panel with its ordinate axis on the right. The inset presents EDS spectra obtained from the regions identified in (a). The thickness versus y position obtained from the AFM is also plotted for comparison.

APPENDIX B: SEM/EDS CHARACTERIZATION

It is noteworthy that the surface roughness of the Ge layer (the one with which the AFM tip interacts) is uniform all over the sample, showing grains in the nanometric scale, with an average area around 1100 nm^2. One can observe this morphology in the secondary electron SEM image in Fig. 9(a), which is somewhat similar to the single Pb layers deposited on different conditions shown in Refs. [95–97].

The elemental composition of a given material can be obtained from its EDS spectra [98]. As the detected energy intensity depends on the initial electron beam energy and the average volume of the droplet-shaped interaction region, EDS may also be employed to estimate the film thickness [70,99–102]. Most authors use the relation $I_f/I_s \sim d$, where I_s (I_f) is the peak intensity of the substrate (film), to obtain the thickness. One way to determine d is to scan the incident electron beam energy to identify at which value the generation of x rays is confined only to the sample film [99]. Then a calibrated curve can be generated from known thicknesses to calculate the thickness of unknown samples. In our case, we kept the acceleration voltage constant at 5 kV, which is large enough to interact with all different layers, including the substrate, and use the Pb/Ge intensity ratio to map the relative profile of the Pb layer along the gradient thickness of the film.

Thus, we chose the same positions where the AFM imaging was performed and monitored the relative heights of the x-ray peaks of the three main elements, assuming that the initial energy of the electron beam penetrates deeply enough to interact with all layers concomitantly. The inset in Fig. 9(b) shows the five spectra for the different regions indicated in Fig. 1(a) in the range 1.08 keV–2.60 keV, where one can identify the Ge-Lα (1.188 keV), Si-Kα (1.739 keV), and Pb-Mα (2.342 keV) characteristic radiation [103,104]. Since the Ge layer is uniform, its peak height is constant for all vertical positions. As expected, the peak height related to Pb decreases as the thickness decreases, as indicated in the zoom up in the center of the graph. Conversely, a higher signal due to Si is obtained as the superconducting film becomes thinner as an indication that the electron beam interacts more with the substrate. Black arrows were added to the peaks to indicate the decrease in thickness. In contrast to the previous works cited, we use the intensity peak ratio between Pb/Ge, which is directly proportional to d, to represent the relative thickness variation as depicted in the main panel of Fig. 9(b). The error bars were taken as 5% for the Pb/Ge ratio based on the relative error of the element amounts. One can observe that the data follows the general behavior of the thickness determined by AFM despite the different scale. Therefore, this data confirms the general behavior of the nonlinear curve for the thickness variation.

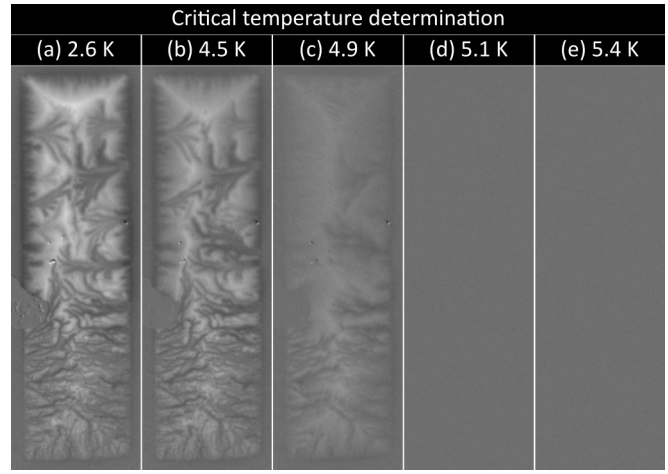

FIG. 10. MO images of the wedge-shaped Pb film as the temperature is risen after a field-cooling procedure up to the lowest temperature, then the field is set to zero. These images demonstrate the flux distribution as captured at (a) 2.6 K, (b) 4.5 K, (c) 4.9 K, (d) 5.1 K, and (e) 5.4 K.

APPENDIX C: CRITICAL TEMPERATURE DETERMINATION BY MOI

MOI allows the determination of the critical temperature of a superconducting specimen. This is the case because MOI can only distinguish between the sample region and free space under the sample applied magnetic field due to the shielding properties of the superconductor. Therefore, if a MO image shows no contrast highlighting the region where the superconductor is located, the sample is in the normal state. Figure 10 presents MO images of the investigated wedge-shaped Pb film. To perform these measurements, the sample was first field cooled to 2.6 K under an applied magnetic field of 20 Oe. Then, the field is set to zero and the temperature was progressively raised while a series of MO images were recorded. This procedure leads to the determination of $T_c^{\mathrm{MOI}} = (5.1 \pm 0.1)$ K, as Fig. 10(d) no longer allows the distinction of the sample region. Importantly, contrast is lost uniformly across the film. Therefore, the thermal contact between the Pb film and the cold finger in the experimental setup is uniform throughout the sample.

[1] G. Wendin, Rep. Prog. Phys. **80**, 106001(2017).
[2] M. Kjaergaard, M. E. Schwartz, J. Braumüller, P. Krantz, J. I.-J. Wang, S. Gustavsson, and W. D. Oliver, Annu. Rev. Condens. Matter Phys. **11**, 369 (2020).
[3] R. H. Hadfield, Nat. Photon. **3**, 696 (2009).
[4] C. M. Natarajan, M. G. Tanner, and R. H. Hadfield, Supercond. Sci. Technol. **25**, 063001 (2012).
[5] S. Franssila, *Introduction to Microfabrication*, 2nd ed. (Wiley Online Library, New York, 2010), pp. 1–518.
[6] D. Luna-Moreno and D. Monzón-Hernández, Appl. Surf. Sci. **253**, 8615 (2007).
[7] K. Yamamura, S. Shimada, and Y. Mori, CIRP Annals **57**, 567 (2008).
[8] Y.-O. Choi, N.-H. Kim, J.-S. Park, and W.-S. Lee, Mater. Sci. Eng. B **171**, 73 (2010).
[9] B. Wang, X. Fu, S. Song, H. O. Chu, D. Gibson, C. Li, Y. Shi, and Z. Wu, Coatings **8**, 325 (2018).
[10] S.-G. Kim, Q. Hu, K.-B. Nam, M. J. Kim, and J.-B. Yoo, Chem. Phys. Lett. **698**, 157 (2018).
[11] E. Knehr, M. Ziegler, S. Linzen, K. Ilin, P. Schanz, J. Plentz, M. Diegel, H. Schmidt, E. Il'ichev, and M. Siegel, J. Vac. Sci. Technol. A **39**, 052401 (2021).
[12] R. Zarnetta, R. Takahashi, M. L. Young, A. Savan, Y. Furuya, S. Thienhaus, B. Maaß, M. Rahim, J. Frenzel, H. Brunken, Y. S. Chu, V. Srivastava, R. D. James, I. Takeuchi, G. Eggeler, and A. Ludwig, Adv. Funct. Mater. **20**, 1917 (2010).

[13] A. Ludwig, npj Comput. Mater. **5**, 70 (2019).
[14] J. Yuan, Q. Chen, K. Jiang, Z. Feng, Z. Lin, H. Yu, G. He, J. Zhang, X. Jiang, X. Zhang, Y. Shi, Y. Zhang, M. Qin, Z. G. Cheng, N. Tamura, Y. feng Yang, T. Xiang, J. Hu, I. Takeuchi, K. Jin *et al.*, Nature (London) **602**, 431 (2022).
[15] V. Palmisano, M. Filippi, A. Baldi, M. Slaman, H. Schreuders, and B. Dam, Int. J. Hydrogen Energy **35**, 12574 (2010).
[16] S. Hiromasa, O. Takahiro, M. Takumi, and S. Shogo, Front. Nanotechnol. **3**, 70 (2021).
[17] F. Born, M. Siegel, E. K. Hollmann, H. Braak, A. A. Golubov, D. Y. Gusakova, and M. Y. Kupriyanov, Phys. Rev. B **74**, 140501(R) (2006).
[18] E. Antropov, M. S. Kalenkov, J. Kehrle, V. I. Zdravkov, R. Morari, A. Socrovisciuc, D. Lenk, S. Horn, L. R. Tagirov, A. D. Zaikin, A. S. Sidorenko, H. Hahn, and R. Tidecks, Supercond. Sci. Technol. **26**, 085003 (2013).
[19] Q. Du, M. D. Gunzburger, and J. S. Peterson, Phys. Rev. B **51**, 16194 (1995).
[20] S. J. Chapman, Q. Du, and M. D. Gunzburger, Z. Angew. Math. Phys. **47**, 410 (1996).
[21] E. Sardella and E. H. Brandt, Supercond. Sci. Technol. **23**, 025015 (2010).
[22] Y. Lu, Z. Jing, H. Yong, and Y. Zhou, Proc. R. Soc. A **472**, 20160469 (2016).
[23] P. Sabatino, G. Carapella, and M. Gombos, J. Appl. Phys. **112**, 083909 (2012).
[24] V. N. Gladilin, J. Ge, J. Gutierrez, M. Timmermans, J. Van de Vondel, J. Tempere, J. T. Devreese, and V. V. Moshchalkov, New J. Phys. **17**, 063032 (2015).
[25] F. Hengstberger, M. Eisterer, and H. W. Weber, Appl. Phys. Lett. **96**, 022508 (2010).
[26] A. Mogro-Campero, L. G. Turner, E. L. Hall, N. Lewis, L. A. Peluso, and W. E. Balz, Supercond. Sci. Technol. **3**, 62 (1990).
[27] S. R. Foltyn, P. N. Arendt, Q. X. Jia, H. Wang, J. L. MacManus-Driscoll, S. Kreiskott, R. F. DePaula, L. Stan, J. R. Groves, and P. C. Dowden, Appl. Phys. Lett. **82**, 4519 (2003).
[28] S. Onori and A. Rogani, Physica B+C **132**, 217 (1985).
[29] R. D. Chaudhari and J. B. Brown, Phys. Rev. **139**, A1482 (1965).
[30] K. Il'in, D. Rall, M. Siegel, A. Engel, A. Schilling, A. Semenov, and H.-W. Huebers, Physica C **470**, 953 (2010).
[31] E. F. Talantsev and J. L. Tallon, Nat. Commun. **6**, 7820 (2015).
[32] J. Brisbois, V. N. Gladilin, J. Tempere, J. T. Devreese, V. V. Moshchalkov, F. Colauto, M. Motta, T. H. Johansen, J. Fritzsche, O.-A. Adami, N. D. Nguyen, W. A. Ortiz, R. B. G. Kramer, and A. V. Silhanek, Phys. Rev. B **95**, 094506 (2017).
[33] C. P. Bean, Phys. Rev. Lett. **8**, 250 (1962).
[34] Y. B. Kim, C. F. Hempstead, and A. R. Strnad, Phys. Rev. **129**, 528 (1963).
[35] W. A. Fietz, M. R. Beasley, J. Silcox, and W. W. Webb, Phys. Rev. **136**, A335 (1964).
[36] L. Burger, I. S. Veshchunov, T. Tamegai, A. Silhanek, S. Nagasawa, M. Hidaka, and B. Vanderheyden, Supercond. Sci. Technol. **32**, 125010 (2019).
[37] L. Jiang, C. Xue, L. Burger, B. Vanderheyden, A. V. Silhanek, and Y.-H. Zhou, Phys. Rev. B **101**, 224505 (2020).
[38] M. Motta, L. Burger, L. Jiang, J. D. Gonzalez Acosta, Ž. Jelić, F. Colauto, W. A. Ortiz, T. H. Johansen, M. V. Milošević, C. Cirillo, C. Attanasio, C. Xue, A. V. Silhanek, and B. Vanderheyden, Phys. Rev. B **103**, 224514 (2021).
[39] D. A. D. Chaves, I. M. de Araújo, D. Carmo, F. Colauto, A. A. M. de Oliveira, A. M. H. de Andrade, T. H. Johansen, A. V. Silhanek, W. A. Ortiz, and M. Motta, Appl. Phys. Lett. **119**, 022602 (2021).
[40] E. H. Brandt, Phys. Rev. B **55**, 14513 (1997).
[41] E. H. Brandt, Phys. Rev. B **49**, 9024 (1994).
[42] J. R. Clem and A. Sanchez, Phys. Rev. B **50**, 9355 (1994).
[43] E. H. Brandt, Phys. Rev. B **50**, 4034 (1994).
[44] E. Zeldov, J. R. Clem, M. McElfresh, and M. Darwin, Phys. Rev. B **49**, 9802 (1994).
[45] E. Altshuler and T. H. Johansen, Rev. Mod. Phys. **76**, 471 (2004).
[46] D. V. Denisov, D. V. Shantsev, Y. M. Galperin, E. M. Choi, H. S. Lee, S. I. Lee, A. V. Bobyl, P. E. Goa, A. A. F. Olsen, and T. H. Johansen, Phys. Rev. Lett. **97**, 077002 (2006).
[47] F. Colauto, M. Motta, and W. A. Ortiz, Supercond. Sci. Technol. **34**, 013002 (2021).
[48] V. V. Yurchenko, T. H. Johansen, and Y. M. Galperin, Low Temp. Phys. **35**, 619 (2009).
[49] J. I. Vestgården, T. H. Johansen, and Y. M. Galperin, Low Temp. Phys. **44**, 460 (2018).
[50] J. I. Vestgården, D. V. Shantsev, Y. M. Galperin, and T. H. Johansen, Phys. Rev. B **84**, 054537 (2011).
[51] S. Blanco Alvarez, J. Brisbois, S. Melinte, R. B. G. Kramer, and A. V. Silhanek, Sci. Rep. **9**, 3659 (2019).
[52] M. Menghini, R. J. Wijngaarden, A. V. Silhanek, S. Raedts, and V. V. Moshchalkov, Phys. Rev. B **71**, 104506 (2005).
[53] M. Motta, F. Colauto, J. I. Vestgården, J. Fritzsche, M. Timmermans, J. Cuppens, C. Attanasio, C. Cirillo, V. V. Moshchalkov, J. Van de Vondel, T. H. Johansen, W. A. Ortiz, and A. V. Silhanek, Phys. Rev. B **89**, 134508 (2014).
[54] I. S. Abal'osheva, A. Abal'oshev, M. Cieplak, L. Zhu, and C.-L. Chien, Acta Phys. Pol. A **118**, 396 (2010).
[55] J. I. Vestgarden, Y. M. Galperin, and T. H. Johansen, arXiv:1309.6463.
[56] I. Abaloszewa, M. Z. Cieplak, and A. Abaloszew, arXiv:2207.12811.
[57] L. E. Helseth, R. W. Hansen, E. I. Il'yashenko, M. Baziljevich, and T. H. Johansen, Phys. Rev. B **64**, 174406 (2001).
[58] L. E. Helseth, A. G. Solovyev, R. W. Hansen, E. I. Il'yashenko, M. Baziljevich, and T. H. Johansen, Phys. Rev. B **66**, 064405 (2002).
[59] G. Shaw, J. Brisbois, L. B. G. L. Pinheiro, J. Müller, S. Blanco Alvarez, T. Devillers, N. M. Dempsey, J. E. Scheerder, J. Van de Vondel, S. Melinte, P. Vanderbemden, M. Motta, W. A. Ortiz, K. Hasselbach, R. B. G. Kramer, and A. V. Silhanek, Rev. Sci. Instrum. **89**, 023705 (2018).
[60] P. Thévenaz, U. E. Ruttimann, and M. Unser, IEEE Trans. Image Process. **7**, 27 (1998).
[61] C. A. Schneider, W. S. Rasband, and K. W. Eliceiri, Nat. Meth. **9**, 671 (2012).
[62] A. Y. Meltzer, E. Levin, and E. Zeldov, Phys. Rev. Appl. **8**, 064030 (2017).
[63] D. V. Denisov, A. L. Rakhmanov, D. V. Shantsev, Y. M. Galperin, and T. H. Johansen, Phys. Rev. B **73**, 014512 (2006).
[64] R. Mints and A. Rakhmanov, Rev. Mod. Phys. **53**, 551 (1981).
[65] F. S. Portela, L. T. Corredor, P. Barrozo, S.-G. Jung, G. Zhang, J. Vanacken, V. V. Moshchalkov, and J. A. Aguiar, Supercond. Sci. Technol. **28**, 034001 (2015).
[66] C. P. Bean, Rev. Mod. Phys. **36**, 31 (1964).

[67] T. Schuster, H. Kuhn, and E. H. Brandt, Phys. Rev. B **54**, 3514 (1996).
[68] M. I. Valerio-Cuadros, D. A. D. Chaves, F. Colauto, A. A. M. d. Oliveira, A. M. H. d. Andrade, T. H. Johansen, W. A. Ortiz, and M. Motta, Mater. **14**, 7274 (2021).
[69] J. Brisbois, O.-A. Adami, J. I. Avila, M. Motta, W. A. Ortiz, N. D. Nguyen, P. Vanderbemden, B. Vanderheyden, R. B. G. Kramer, and A. V. Silhanek, Phys. Rev. B **93**, 054521 (2016).
[70] L. B. L. G. Pinheiro, M. Motta, F. Colauto, T. H. Johansen, E. Bellingeri, C. Bernini, C. Ferdeghini, and W. A. Ortiz, IEEE Trans. Appl. Supercond. **29**, 1 (2019).
[71] E. H. Brandt, M. V. Indenbom, and A. Forkl, Europhys. Lett. **22**, 735 (1993).
[72] S. R. Foltyn, P. Tiwari, R. C. Dye, M. Q. Le, and X. D. Wu, Appl. Phys. Lett. **63**, 1848 (1993).
[73] R. P. Huebener and A. Seher, Phys. Rev. **181**, 710 (1969).
[74] C. P. Poole-Jr, H. A. Farach, R. J. Creswick, and R. Prozorov, in *Superconductivity*, 2nd ed. (Academic Press, The Netherlands, 2007), Vol. 1, p. 646.
[75] C. Jooss, J. Albrecht, H. Kuhn, S. Leonhardt, and H. Kronmüller, Rep. Prog. Phys. **65**, 651 (2002).
[76] M. Strongin, R. S. Thompson, O. F. Kammerer, and J. E. Crow, Phys. Rev. B **1**, 1078 (1970).
[77] Y. Ivry, C.-S. Kim, A. E. Dane, D. De Fazio, A. N. McCaughan, K. A. Sunter, Q. Zhao, and K. K. Berggren, Phys. Rev. B **90**, 214515 (2014).
[78] F. E. Harper and M. Tinkham, Phys. Rev. **172**, 441 (1968).
[79] M. Tinkham, Phys. Rev. **129**, 2413 (1963).
[80] G. D. Cody and R. E. Miller, Phys. Rev. **173**, 481 (1968).
[81] T. Takayama, T. Ōgushi, and Y. Shibuya, J. Phys. Soc. Jpn. **30**, 1083 (1971).
[82] B. L. Brandt, R. D. Parks, and R. D. Chaudhari, J. Low Temp. Phys. **4**, 41 (1971).
[83] J. Albrecht, A. T. Matveev, J. Strempfer, H.-U. Habermeier, D. V. Shantsev, Y. M. Galperin, and T. H. Johansen, Phys. Rev. Lett. **98**, 117001 (2007).
[84] Z. Jing, H. Yong, and Y. Zhou, Supercond. Sci. Technol. **29**, 105001 (2016).
[85] T. H. Johansen, M. Baziljevich, D. V. Shantsev, P. E. Goa, Y. M. G. pe rin, W. N. Kang, H. J. Kim, E. M. Choi, M.-S. Kim, and S. I. Lee, Europhys. Lett. **59**, 599 (2002).
[86] M. S. Welling, R. J. Westerwaal, W. Lohstroh, and R. J. Wijngaarden, Physica C **411**, 11 (2004).
[87] J. I. Vestgarden, D. V. Shantsev, Y. M. Galperin, and T. H. Johansen, Sci. Technol. **26** 055012 (2013).
[88] T. H. Johansen, M. Baziljevich, D. V. Shantsev, P. E. Goa, Y. M. Galperin, W. N. Kang, H. J. Kim, E. M. Choi, M. S. Kim, and S. I. Lee, Supercond. Sci. Technol. **14**, 726 (2001).
[89] E.-M. Choi, V. V. Yurchenko, T. H. Johansen, H.-S. Lee, J. Y. Lee, W. N. Kang, and S.-I. Lee, Supercond. Sci. Technol. **22**, 015011 (2009).
[90] L. B. Pinheiro, M. Caputo, C. Cirillo, C. Attanasio, T. H. Johansen, W. A. Ortiz, A. V. Silhanek, and M. Motta, Low Temp. Phys. **46**, 365 (2020).
[91] A. J. Qviller, V. V. Yurchenko, K. Eliassen, J. I. V. rden, T. H. Johansen, M. R. Nevala, I. J. Maasilta, K. Senapati, and R. C. Budhani, Physica C **470**, 897 (2010).
[92] D. L. Smith, *Thin-Film Deposition: Principles and Practice* (McGraw-Hill Education, New York, 1995).
[93] Novaetech S.r.l., Quartz crystal microbalance, https://openqcm.com/openqcm, 2021 (Online; accessed 8-December-2021).
[94] P. Walker and W. H. Tarn, *CRC Handbook of Metal Etchants* (CRC Press, Boca Raton, 1990), p. 1415.
[95] A. Perrone, F. Gontad, A. Lorusso, M. Di Giulio, E. Broitman, and M. Ferrario, Nucl. Instrum. Meth. Phys. Res. A **729**, 451 (2013).
[96] A. Lorusso, F. Gontad, E. Broitman, E. Chiadroni, and A. Perrone, Thin Solid Films **579**, 50 (2015).
[97] E. Broitman, F. J. Flores-Ruiz, M. Di Giulio, F. Gontad, A. Lorusso, and A. Perrone, J. Vac. Sci. Technol. A **34**, 021505 (2016).
[98] Ludwig Reimer, *Electron Scattering and Diffusion* (Springer, Berlin, 1985), pp. 1–388.
[99] R. Pascual, L. R. Cruz, C. L. Ferreira, and D. T. Gomes, Thin Solid Films **185**, 279 (1990).
[100] F. L. Ng, J. Wei, F. K. Lai, and K. L. Goh, Appl. Surf. Sci. **252**, 3972 (2006).
[101] L. Zhuang, S. Bao, R. Wang, S. Li, L. Ma, and D. Lv, in *2009 International Conference on Applied Superconductivity and Electromagnetic Devices* (IEEE, New York, 2009), pp. 142–144.
[102] K. W. Habiger and C. Stein, Thin Solid Films **215**, 108 (1992).
[103] J. I. Goldstein, D. E. Newbury, P. Echlin, D. C. Joy, C. E. Lyman, E. Lifshin, L. Sawyer, and J. R. Michael, *Scanning Electron Microscopy and X-Ray Microanalysis*, 3rd ed. (Springer Science, New York, 2003).
[104] S. J. B. Reed, *Electron Microprobe Analysis and Scanning Electron Microscopy in Geology*, 2nd ed. (Cambridge University Press, Cambridge, 2005).

Correction: The fourth sentence of the abstract contained an erroneous duplication of words introduced during the production process and has been fixed.